



# Preparation and capacitance behavior of manganese oxide hollow structures with different morphologies *via* template-engaged redox etching

Yan Gu<sup>a,b</sup>, Jianwei Cai<sup>a,b</sup>, Mingze He<sup>a,b</sup>, Liping Kang<sup>a,b</sup>, Zhibin Lei<sup>a,b</sup>, Zong-Huai Liu<sup>a,b,\*</sup>

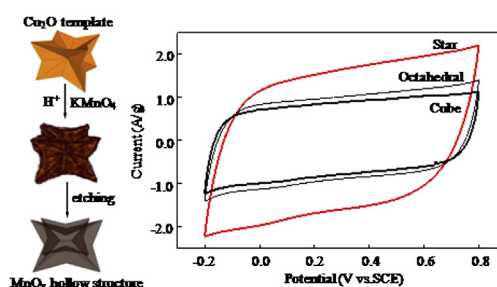
<sup>a</sup> Key Laboratory of Applied Surface and Colloid Chemistry, Shaanxi Normal University, Ministry of Education, Xi'an 710062, PR China

<sup>b</sup> School of Materials Science and Engineering, Shaanxi Normal University, Xi'an 710062, PR China

## HIGHLIGHTS

- Amorphous manganese oxide hollow interiors are prepared by a redox etching process.
- Star-shaped amorphous manganese oxide hollow interiors show large specific surface area of  $198 \text{ m}^2 \text{ g}^{-1}$ .
- Capacitance of amorphous manganese oxide electrodes is connects with the specific surface area.
- Star-shaped amorphous manganese oxide hollow star electrode exhibits high specific capacitance of  $366 \text{ F g}^{-1}$ .

## GRAPHICAL ABSTRACT



## ARTICLE INFO

### Article history:

Received 24 November 2012

Received in revised form

25 February 2013

Accepted 25 March 2013

Available online 1 April 2013

### Keywords:

$\text{Cu}_2\text{O}$  sacrificial templates

Redox etching

$\text{MnO}_2$  hollow structure

Capacitance

## ABSTRACT

A variety of amorphous manganese oxide electrode materials with uniform nonspherical hollow interiors are prepared *via* sacrificial template-engaged redox etching of the corresponding shape-controlled  $\text{Cu}_2\text{O}$  nanocrystals in  $\text{KMnO}_4$  aqueous solution at room temperature. The obtained materials are characterized by X-ray diffraction, X-ray photoelectron spectroscopy, scanning electron microscopy, transmission electron microscopy and  $\text{N}_2$  adsorption–desorption. The amorphous manganese oxide hollow materials not only well inherit the size and shape of  $\text{Cu}_2\text{O}$  nonspherical precursor, but also show a manganese average oxidation state of 3.7 and large specific surface area (about  $198 \text{ m}^2 \text{ g}^{-1}$ ). The electrochemical measurements show that the capacitance of the as-prepared amorphous manganese oxide electrode materials with uniform nonspherical hollow interiors is connects with their specific surface area. The amorphous manganese oxide star hollow architecture exhibits not only high specific capacitance of  $366 \text{ F g}^{-1}$  at a scan rate of  $5 \text{ mV s}^{-1}$ , but also relatively good cycle stability (93.1% capacitance retention after 1000 cycles at a scan rate of  $20 \text{ mV s}^{-1}$ ), which make it have a potential application as a supercapacitor electrode material.

© 2013 Published by Elsevier B.V. All rights reserved.

## 1. Introduction

Electrochemical capacitor (EC) has emerged with wide application potential because it can provide higher energy density than

conventional capacitors, and greater power density and longer cycling life than batteries through the use of high-surface-area electrodes and fast surface-charge-storage processes, which bridges the gap between conventional capacitors and batteries [1–3]. According to the mechanism of the energy storage, the electrochemical capacitor is classified as electric double-layer capacitor (EDLC) and faradaic pseudocapacitor [4, 5]. The double-layer capacitor is usually composed of the electrodes with high-surface-area because the non-faradaic capacitance of the electric

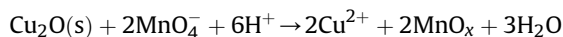
\* Corresponding author. School of Materials Science and Engineering, Shaanxi Normal University, Xi'an 710062, PR China. Tel.: +86 29 81530706; fax: +86 29 81530702.

E-mail address: [zhliu@snnu.edu.cn](mailto:zhliu@snnu.edu.cn) (Z.-H. Liu).

double-layer stores energy by charge separation formed at the interface between the electrode and the electrolyte [5,6]. On the other hand, the faradaic pseudocapacitor based on transition metal oxides has attracted significant attention owing to its high specific capacitance, excellent reversibility and long cycle life [4,5,7]. Among these transition metal oxides, amorphous hydrated ruthenium oxide with remarkable pseudocapacitive behavior is one of the most attractive candidates for the electrode of electrochemical capacitors [7,8]. However, the high cost of ruthenium has limited its commercial use. Therefore, the investigate research for the cheaper metal oxides with equivalent characteristics is attracting attention.

Among the transition metal oxides with various valence states, manganese oxide is one of the most promising pseudocapacitance electrode materials due to its high specific capacitance, environmental compatibility and cost effectiveness [9,10]. Up to now, many manganese oxides with various structures and morphologies have been prepared *via* electrochemical and chemical routes, and their electrochemical properties have been investigated. The investigated materials mainly focus on the amorphous or poorly crystallized manganese oxides, single-crystalline manganese oxides and manganese oxide thin films because these material cathodes show ideally capacitive behavior such as large capacity, good electrochemical reversibility and high pulse-power property in a potential window of 1.0 V in Na<sub>2</sub>SO<sub>4</sub> solution [11–18]. Moreover, it is well-known that manganese oxides with hollow structure have attracted considerable interest owing to its unique properties, such as large surface area, well-defined morphology, low density, and high energy storage ability [19–24]. In the past few years, a series of manganese oxides with hollow structure, including hollow nanospheres [20,23–25], nanotubes [26,27], hollow urchins [28,29], and hollow polyhedrons [30] have been synthesized. In general, two fabrication methods can be used to prepare these manganese oxides with hollow structure, which are a hard template method and template-free technology. Although the manganese oxides with hollow structure can be fabricated by hard template method, the removal of these templates such as mono-dispersed silica [21] or polycrystalline [31] by either thermal (sintering) or chemical (etching) methods is very complicated and energy-consuming, only the manganese oxide hollow structures with spherical or tubular morphologies can be obtained by a Ostwald ripening process [21,31], self-assembling [26] or Kirkendall effect [32]. Therefore, it is expected to develop a facile approach for preparation manganese oxides with hollow structure and different morphologies *via* nonspherical sacrificial templates. Compared with the widely reported templates, Cu<sub>2</sub>O is one of the best corrosion-prone candidate sacrificial templates [33,34] because it has many advantages, such as the diversity in crystal morphology, low reduction potential (Cu<sup>2+</sup>/Cu<sub>2</sub>O = 0.203 V, vs SHE, SHE is abbreviated for standard hydrogen electrode) [35] and low prefabrication cost [36,37].

In the present work, a facile one-step approach was developed to prepare a variety of amorphous manganese oxide electrode materials with different morphologies and uniform hollow structure *via* sacrificial template-engaged redox etching of the corresponding shape-controlled Cu<sub>2</sub>O nanocrystals in KMnO<sub>4</sub> solution at room temperature. Because the Cu<sup>2+</sup>/Cu<sub>2</sub>O standard reduction potential (0.203 V, vs SHE) is much lower than that of KMnO<sub>4</sub>/MnO<sub>2</sub> (1.679 V vs SHE), the redox reaction between Cu<sub>2</sub>O template and MnO<sub>4</sub><sup>−</sup> ions is thermodynamically feasible. Cu<sub>2</sub>O nanocrystals in suspension could be oxidized by MnO<sub>4</sub><sup>−</sup> ions at room temperature according to the following redox reaction:



and manganese oxide hollow structures with different morphologies were obtained by the complete consumption of Cu<sub>2</sub>O template. The schematic formation process of the manganese oxide

hollow structures with different morphologies is illustrated in Fig. 1. This bottom–up approach could be used to controllably prepare metal oxide hollow structures with different morphologies and sizes. The as-prepared amorphous manganese oxide hollow structure with star morphology shows large specific surface area and an ideal capacitive behavior.

## 2. Experimental

### 2.1. Material preparation

CuCl<sub>2</sub>·2H<sub>2</sub>O, NaOH, PVP (polyvinylpyrrolidone), CuSO<sub>4</sub>·5H<sub>2</sub>O, Na<sub>2</sub>CO<sub>3</sub>, C<sub>6</sub>H<sub>8</sub>O<sub>6</sub> (ascorbic acid), C<sub>6</sub>H<sub>5</sub>Na<sub>3</sub>O<sub>7</sub> (sodium citrate), C<sub>6</sub>H<sub>12</sub>O<sub>6</sub> (glucose) and C<sub>2</sub>H<sub>6</sub>O (ethanol) were obtained from Chemical Reagent Ltd., China, in an analytical purity and used without further purification. Deionized water was used throughout the experiments.

#### 2.1.1. Preparation of Cu<sub>2</sub>O nonspherical templates

Cu<sub>2</sub>O nanocubes were synthesized by the report method [36]. In a typical procedure, NaOH solution (2.0 mol L<sup>−1</sup>, 5.0 ml) was added dropwise into CuCl<sub>2</sub> solution (0.01 mol L<sup>−1</sup>, 50 ml) at 55 °C. After stirring for 0.5 h, ascorbic acid solution (0.6 mol L<sup>−1</sup>, 5.0 mL) was added dropwise into the above solution. A turbid red liquid was gradually formed and the mixture was aged for 3 h, the resulting precipitate was collected by centrifugation and decanting, followed by washing with distilled water and absolute ethanol, and finally dried in vacuum at room temperature for 12 h, Cu<sub>2</sub>O nanocubes were obtained. Cu<sub>2</sub>O octahedrons were prepared by above similar method except adding given amounts of PVP (*M<sub>w</sub>* = 30,000) immediately after dropwising the NaOH solution into the CuCl<sub>2</sub> solution. Star-shaped Cu<sub>2</sub>O structure was synthesized *via* reducing the copper-citrate complex [37]. Typically, a mixture solution of 4.0 ml CuSO<sub>4</sub> (0.68 mol L<sup>−1</sup>), 4.0 ml sodium citrate (0.74 mol L<sup>−1</sup>), 4.0 ml anhydrous sodium carbonate (1.2 mol L<sup>−1</sup>) and 5.6 ml glucose (1.0 mol L<sup>−1</sup>) was diluted to 80 ml with deionized water, and then aged at 80 °C for 3 h. The obtained colloid solution was centrifuged, washed with deionized water and followed by ethanol, the star-shaped Cu<sub>2</sub>O structure was obtained.

#### 2.1.2. Preparation of amorphous manganese oxide hollow structures

0.6 mmol Cu<sub>2</sub>O with different morphologies was added to 400 mL deionized water and stirred for 20 min to obtain a suspension. Then 30 mL of a mixed solution of KMnO<sub>4</sub> (0.05 mol L<sup>−1</sup>) and hydrochloric acid (0.01 mol L<sup>−1</sup>) was dropped into the suspension and stirred for 48 h, the obtained precipitate was collected by several rinse-centrifugation cycles and followed by immersing in ammonia solution (18%) for 10 h to remove the Cu<sub>2</sub>O cores. The resulting product was collected by centrifugation, followed by washing with distilled water and finally dried in vacuum at 60 °C for 12 h, the amorphous manganese oxide hollow structures with different morphologies were obtained.

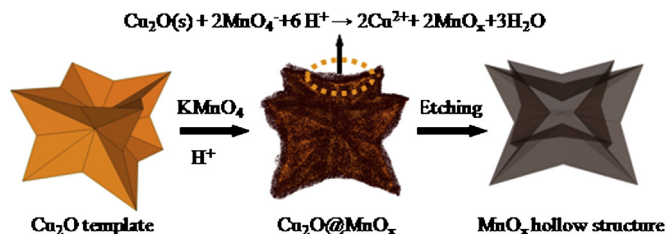
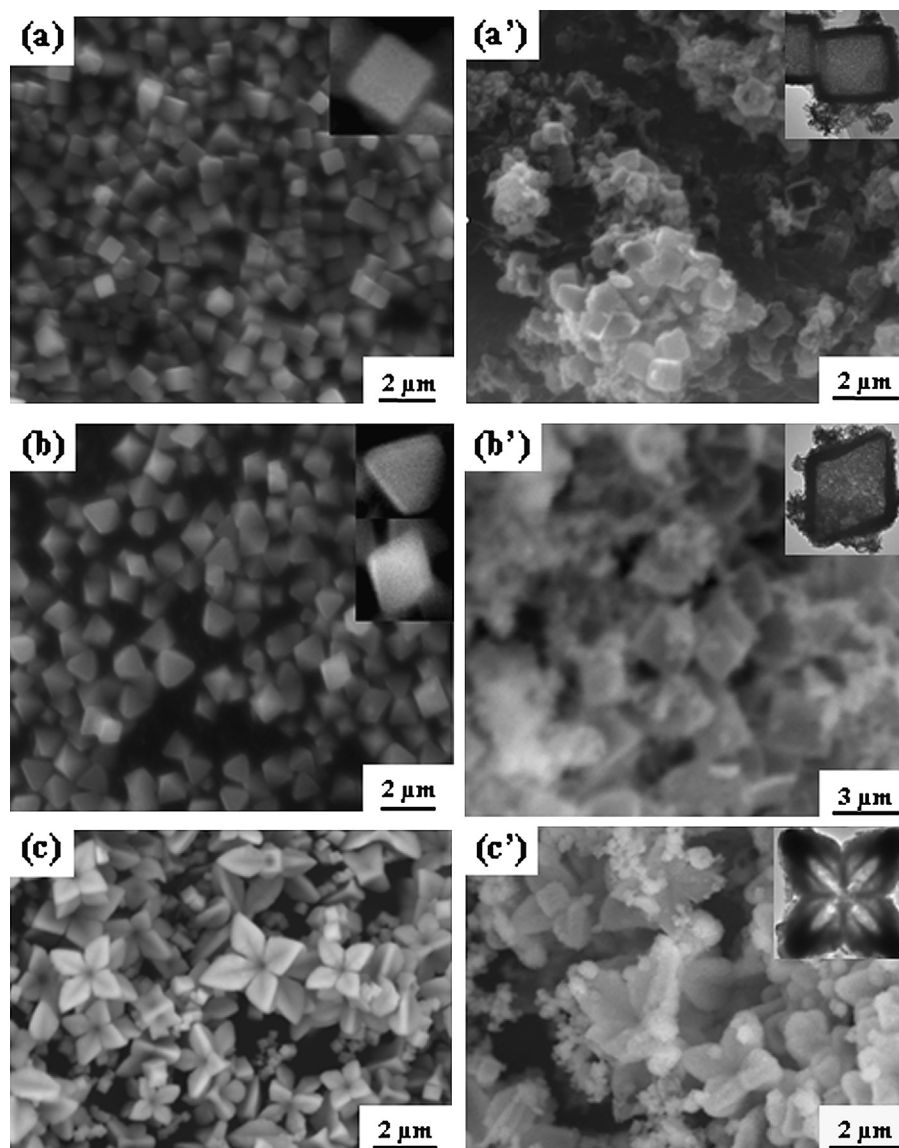


Fig. 1. A schematic formation process of the manganese oxide hollow structure with star morphology by template-engaged coordinating etching of Cu<sub>2</sub>O.



**Fig. 2.** SEM images of  $\text{Cu}_2\text{O}$  polyhedron templates with different morphologies (left) and manganese oxide hollow structures with different morphologies (right): cube (a, a'), octahedron (b, b'), and star (c, c'), respectively. The inset of (a'–c') shows the corresponding TEM images of the manganese oxide hollow structures with different morphologies.

## 2.2. Characterization

X-ray powder diffraction (XRD) pattern was recorded on a D/Max-3c X-ray diffractometer with  $\text{Cu K}\alpha$  radiation operated at 40 kV and 30 mA. X-ray photoelectron spectroscopy (XPS) investigation was performed with a K-Alpha spectrometer using  $\text{Al K}\alpha$  radiation (1486.6 eV) at a power of 150 W (accelerating voltage 12 kV, current 6 mA) in a vacuum of  $8.0 \times 10^{-8}$  mPa. To ensure the accuracy of the data measured, all the binding energies were calibrated relative to the C 1s peak (284.6 eV) from hydrocarbons adsorbed on the surface of the samples [38]. Scanning electron microscopy (SEM) image was taken using a Quanta 200 environmental scanning electron microscopy. Transmission electron microscopy (TEM) image was collected with a JEM-2100 transmission electron microscopy performed at 200 kV. For TEM observation, the sample was dispersed in ethanol by ultrasonic treatment and dropped on a carbon–copper grid. The specific surface area and porosity analyses were obtained using Micromeritics ASAP 2020M equipment. Cu, Mn and K contents were determined by atomic absorption spectrometry (AAS) after the obtained materials were dissolved in a mixed solution of HCl and  $\text{H}_2\text{O}_2$ .

## 2.3. Electrochemical measurement

Electrodes were prepared by mixing active manganese oxide materials (75 wt.%), acetylene black (20 wt.%), and polyvinylidene fluoride (5 wt.%) (The purity of acetylene black and polyvinylidene fluoride are battery grade). The two former constituents were first mixed together to obtain a homogeneous black powder. The polyvinylidene fluoride solution ( $0.02 \text{ g mL}^{-1}$ , in *N*-methyl-ketopyrrolidone) was then added. This resulted in a rubber-like paste, which was brush-coated onto a Ni foam current collector with a definite area of  $2.0 \text{ cm}^2$ . The foam was dried at  $110^\circ\text{C}$  in air for 10 h for the removal of the solvent, and then it was uniaxially pressed to make the electrode material completely adhere with the current collector.

Cyclic voltammetry (CV) and electrochemical impedance spectroscopy (EIS) were measured using a typical three-electrode system. An IviumStat electrochemical workstation (Ivium Technologies BV, Holland) was used for the electrochemical measurement. A beaker type electrochemical cell equipped with manganese oxide based working electrode, a Pt-foil ( $2 \text{ cm}^2$ ) as the counter electrode and saturated calomel electrode (SCE) as the

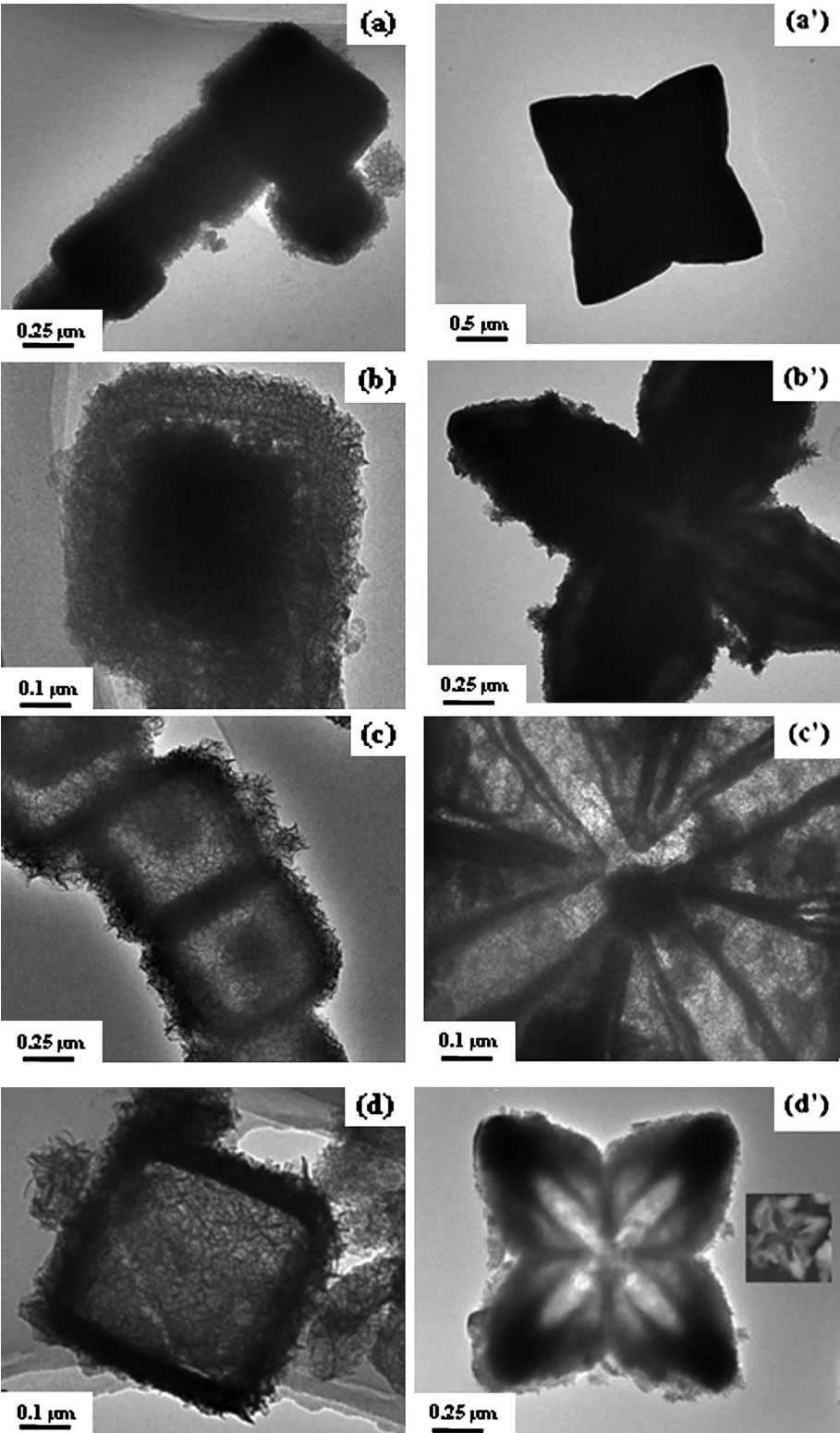


Fig. 3. TEM images of the etching process of  $\text{Cu}_2\text{O}$  cube (left) and  $\text{Cu}_2\text{O}$  star (right).



reference electrode. CV curves were done between  $-0.2$  V and  $0.8$  V in  $1 \text{ mol L}^{-1}$   $\text{Na}_2\text{SO}_4$  electrolyte. The average specific capacitance (SC) was evaluated according to the following equations.

$$C_m = i/mv$$

$$i = \left( \int_{V_a}^{V_c} i(v)dv \right) / (V_c - V_a)$$

where  $m$  is the total mass of the active materials impregnated into nickel foam;  $v$  is the potential scanning rate;  $i$  is the even current response, which is obtained through integrating the area of the curves;  $V_a$  and  $V_c$  represent the lowest and highest voltage, respectively.

### 3. Results and discussion

#### 3.1. Morphology and structure

SEM images of the  $\text{Cu}_2\text{O}$  polyhedral templates and manganese oxide polyhedral nano/mesocage are shown in Fig. 2. It can be seen that the as-prepared polyhedral  $\text{Cu}_2\text{O}$  templates exhibit a range of morphologies including cubes (Fig. 2a), octahedrons (Fig. 2b) and stars (Fig. 2c), indicating that  $\text{Cu}_2\text{O}$  polyhedral precursors with different morphologies can be obtained. The  $\text{Cu}_2\text{O}$  polyhedral precursors with cube and octahedron have an average dimension of about  $0.8$ – $1.2 \text{ }\mu\text{m}$  and well-defined sharp edge and uniform shape, while  $\text{Cu}_2\text{O}$  precursor with star-shape shows symmetric four-pod morphology and an edge length around  $2 \text{ }\mu\text{m}$ . On the other hand, after the suspension of  $\text{Cu}_2\text{O}$  polyhedron precursors with different morphologies is reacted with a mixed solution of  $\text{KMnO}_4$  and hydrochloric acid for 48 h, the obtained manganese oxide precipitates almost maintain the corresponding morphology of the  $\text{Cu}_2\text{O}$  polyhedral precursors (Fig. 2a'–c'). Compared with the  $\text{Cu}_2\text{O}$  polyhedral precursors with differential morphologies, two obvious characterizations can be observed for the obtained manganese oxide hollow architectures. Firstly, the manganese oxide hollow architectures well duplicate the size and shape of the  $\text{Cu}_2\text{O}$  polyhedral precursors with differential morphologies after the  $\text{Cu}_2\text{O}$  core is etched in potassium permanganate solution, and only some slight structural degradation such as collapse or amalgamation is observed during the etching process. Secondly, the rough shell thickness of the obtained manganese oxide hollow architectures is about  $80$ – $100 \text{ nm}$ . For the manganese oxide hollow architecture with cubic morphology, TEM image shows an obvious contrast between the dark edge and pale center, suggesting that a hollow cubic structure with sharp edge and corner is probably obtained (inset in Fig. 2a'), while a perfect interior with a strong contrast difference between the edge (dark) and center (bright) can be observed by TEM image of the manganese oxide octahedral hollow architecture (inset in Fig. 2b'). For the star-shaped manganese oxide mesocage, its void size is also mainly determined by the dimension of the corresponding  $\text{Cu}_2\text{O}$  template (Fig. 2c'). The TEM image clearly shows that the individual star-shaped hollow architecture has darker contrast on the tips and edges and lighter contrast on the cross-shaped diagonal line for each face (inset in Fig. 2c'), suggesting that the star-shaped hollow architecture is highly symmetrical with the corresponding concave cavities inside.

To further determine the pathway of the top–down etching process, the manganese oxide hollow architectures with cubic and star morphologies are further characterized, and the TEM images are shown in Fig. 3. It can be seen that the manganese oxide hollow architectures are gradually formed around the frame of the

sacrificial  $\text{Cu}_2\text{O}$  templates at the initial etching redox reaction stage between  $\text{KMnO}_4$  solution and  $\text{Cu}_2\text{O}$  templates. As the etching redox reaction proceeds, the edge portion of the  $\text{Cu}_2\text{O}$  templates gradually becomes bright compared with its central position (Fig. 3b, b'), suggesting that the manganese oxide hollow architecture is deposited on the frame of the sacrificial  $\text{Cu}_2\text{O}$  templates. The bright portion surface area gradually increases while the hard portion decreases in company with the etching process, and  $\text{Cu}_2\text{O}$  templates nearly dissolve while the manganese oxide hollow structures are finally obtained (Fig. 3c–d, c'–d'). These experimental results indicate that the etching process is carried out by a top–down reaction process, and the manganese oxide hollow structures are formed.

X-ray diffraction patterns of the cubic  $\text{Cu}_2\text{O}$  template, the  $\text{Cu}_2\text{O}@\text{MnO}_x$  intermediate and the cubic hollow manganese oxide are shown in Fig. 4. For the  $\text{Cu}_2\text{O}$  template, all of the diffraction peaks can be perfectly indexed to the cubic phase  $\text{Cu}_2\text{O}$  with lattice constants  $a = 4.270 \text{ }\text{\AA}$ , which are corresponding with the (100), (111), (200), (111) and (220) planes of the cubic phase  $\text{Cu}_2\text{O}$  (JCPDS Card File No. 05-0667) [37] (Fig. 4a). No peaks from other phases are found, suggesting that the as-synthesized  $\text{Cu}_2\text{O}$  template has high purity. As the etching redox reaction proceeds, the diffraction peak of the  $\text{Cu}_2\text{O}@\text{MnO}_x$  intermediate in intensity gradually decreases, suggesting the corrosion of  $\text{Cu}_2\text{O}$  templates via  $\text{KMnO}_4$  redox etching (Fig. 4b). For the manganese oxide hollow architecture, the diffraction peak of the  $\text{Cu}_2\text{O}$  template completely disappears while only gives a plane pattern without pronounced diffraction (Fig. 4c). These results indicate that the as-prepared manganese oxide hollow architecture is amorphous in nature because the synthesis is carried out at room temperature. The atomic absorption analysis results show that the residual Cu content is 1.46% for manganese oxide hollow cube, 1.69% for manganese oxide hollow octahedral, and 1.52% for manganese oxide hollow star, respectively, indicating that the  $\text{Cu}_2\text{O}$  template is nearly etched.

When the manganese oxide material is used as the supercapacitor cathode, the valence of manganese is very important.

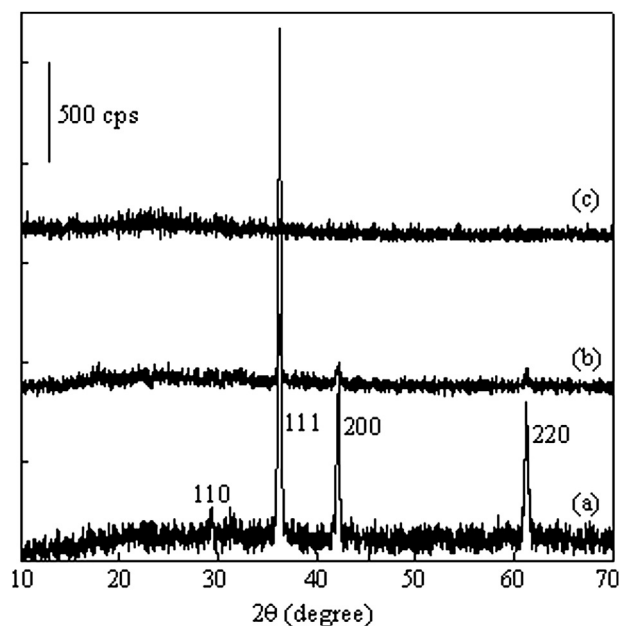


Fig. 4. XRD patterns of the materials at different stages: (a)  $\text{Cu}_2\text{O}$  cube, (b)  $\text{Cu}_2\text{O}@\text{MnO}_x$  intermediate, and (c) manganese oxide cubic hollow structure, respectively.

Therefore, the manganese oxidation state of the synthesized manganese oxide hollow cube is investigated by X-ray photoelectron spectroscopy, and the XPS spectroscopic data for Mn 2p, Mn 3s, and O 1s spectra are shown in Fig. 5. Two peaks at 642 eV and 654.1 eV are observed, which correspond to the binding energies of Mn 2p<sub>3/2</sub> and Mn 2p<sub>1/2</sub> (Fig. 5a). The binding energy values agree well with those of the prepared MnO<sub>2</sub> [39,40], suggesting that a large number of Mn(IV) are existed in the manganese oxide hollow cube. However, it is insufficient to determine the exact manganese oxidation state only from the Mn 2p spectrum because of the broadening or tailing of peaks at lower binding energy [41], and more important information may be obtained by investigating the Mn 3s and O 1s core level spectra.

In general, the Mn 3s core level spectrum usually shows a peak splitting and a doublet due to a parallel spin coupling between the 3s electron and the 3d electron during the photoelectron ejection [42]. For manganese oxide hollow cube, a peak splitting of Mn 3s core level spectrum is observed, and the peak energy separation value ( $\Delta E$ ) is 4.8 eV (Fig. 5b). On the basis of an approximately linear relationship between the splitting width ( $\Delta E$ ) and the Mn oxidation state reported by Toupin group [41], the average oxidation state of Mn is 3.8 for as-prepared manganese oxide hollow cube. This value is similar to that reported for  $\alpha$ -MnO<sub>2</sub> and is consistent with the presence of Mn(III) into the structure [42]. Moreover, the O 1s core level spectrum can be further used to confirm the change of manganese oxidation state during redox switching [16,43]. On the basis of the three oxygen bonds such as water molecule (H–O–H) at 531.8–532.8 eV, hydroxide (Mn–O–H) at 530.5–531.5 eV and oxide (Mn–O–Mn bond, representing the contribution of two species: MnOOH and MnO<sub>2</sub>) at 529.3–530.0 eV [40], the average oxidation state of manganese is calculated from the intensities of the Mn–O–Mn and Mn–O–H components according to the following formula [43]:

$$\text{Manganese oxidation state} = [\text{IV} \cdot (S_{\text{Mn-O-Mn}} - S_{\text{Mn-O-H}}) + \text{III} \cdot S_{\text{Mn-O-H}}] / S_{\text{Mn-O-Mn}}$$

S stands for the signal of the different components for O 1s spectrum. By subtracting the contribution of the hydroxyl group (Mn–OH) and the Mn–O–Mn signal, the Mn average oxidation state of the as-prepared manganese oxide hollow cube is 3.7, which is very close to the result analyzed from Mn 3s core level spectrum (3.8). Therefore, the O 1s core level spectrum also can be used to analyze the average oxidation state of manganese as an effective subsidiary way.

Combining the analysis on Mn 2p and Mn 3s above, the existence of Mn(III)/Mn(IV) mixed valence state can be further confirmed. According to the charge storage mechanism of manganese oxide materials, a mixed valence manganese system is of benefit for the contribution of the capacitance of manganese oxide electrode, because the coexistence of Mn(IV) and Mn(III) may facilitate the formation of more ionic defects, thus may accelerate the kinetics of the surface redox reactions and enhance the transport of charged species and extend the reaction sites from the surface to the subsurface of electrode [44].

### 3.2. Porosity property

The N<sub>2</sub> adsorption–desorption isotherms and the Barrett–Joyner–Halenda (BJH) pore size distribution curves (inset) of manganese oxide hollow structures with different morphologies are presented in Fig. 6. It can be seen that all the isotherms of the three samples belong to type IV according to IUPAC classification [45], indicating the presence of mesopores derived from the self-assembly of 2D nanosheet building blocks. The BET surface areas of the three samples show that the manganese oxide hollow star

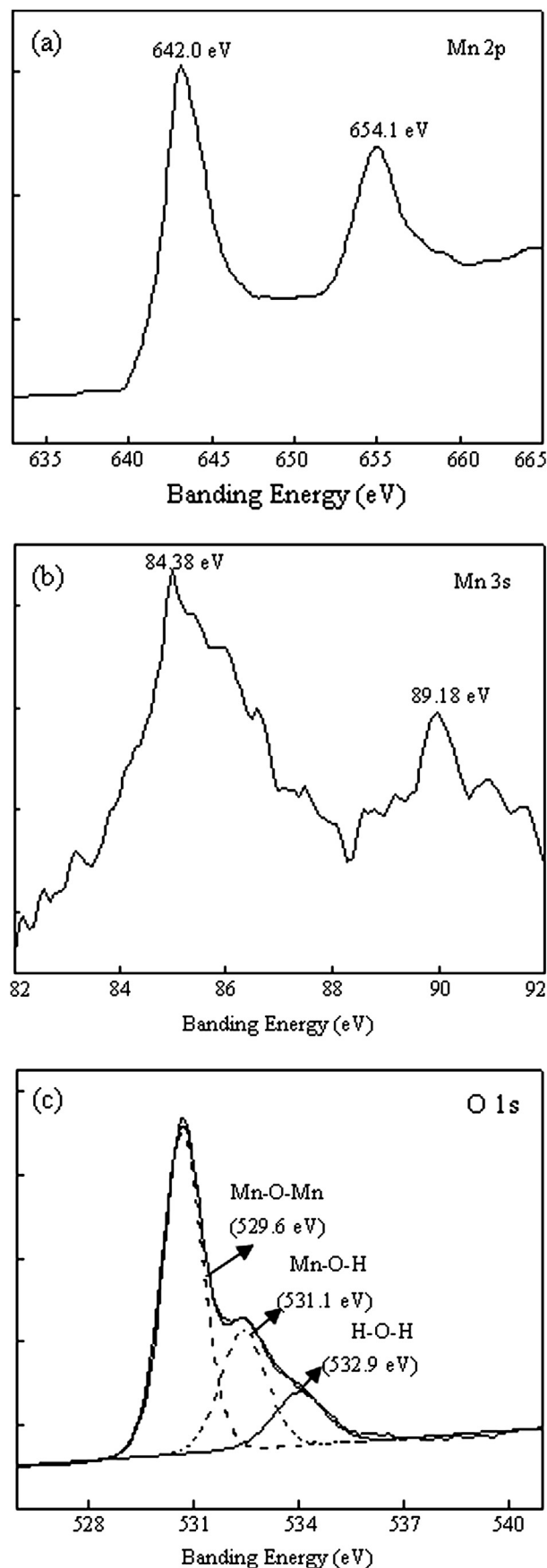


Fig. 5. XPS spectra of the manganese oxide cubic hollow structure: (a) Mn 3s, (b) Mn 2p, and (c) O 1s.

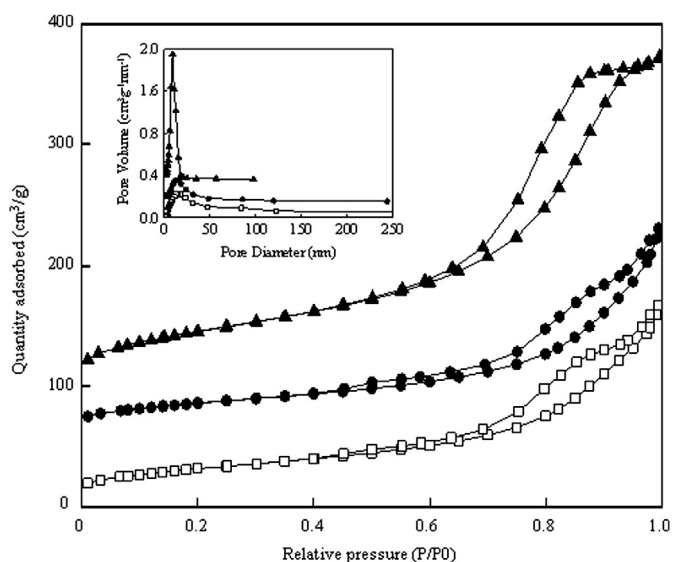


Fig. 6. Nitrogen adsorption–desorption isotherms of the manganese oxide hollow structures with different morphologies: cubes ( $\square$ ), octahedrons ( $\bullet$ ), and stars ( $\blacktriangle$ ), respectively. The inset shows BJH pore size distributions.

possesses the highest surface area ( $198 \text{ m}^2 \text{ g}^{-1}$ ), while both manganese oxide hollow cube and manganese oxide hollow octahedron have relative lower surface area (about  $90 \text{ m}^2 \text{ g}^{-1}$ ). The BJH pore size distributions calculated from the desorption data indicate that the manganese oxide hollow star has a narrow pore size distribution and the average pore diameter is about  $8.0 \text{ nm}$ , indicating the presence of mesopore and micropore. On the other hand, the average pore diameters of manganese oxide hollow cube and manganese oxide hollow octahedron are  $16.4 \text{ nm}$  and  $15.9 \text{ nm}$ , respectively. The smaller average pore size may be explained why the surface area of the manganese oxide hollow star is much larger than that of the two others.

There are only a few reports on mesoporous manganese oxides with hollow structure. He et al. have synthesized the manganese oxide microspheres with hollow structure via a simple hydrothermal method with assistance of  $\text{Fe}^{3+}$  ions [28]. Chen et al. have reported the preparation of mesoporous layered manganese oxide nanospheres with honeycomb and hollow morphologies at room temperature by varying the molar ratio of  $\text{KMnO}_4$  and oleic acid [46]. Tang et al. have prepared mesoporous hierarchical hollow manganese oxide nanospheres with a layered structure via a  $\text{SiO}_2$  templating-assisted hydrothermal process [20]. Lee et al. have reported the preparation of porous  $\text{Mn}_3\text{O}_4$  nanoparticles by using a block copolymer template (Pluronic F127) as a dispersant [47]. In the present work, manganese oxide hollow architecture with both a large surface area and star morphology is prepared. The large specific surface area may be principally ascribed to the hollow inner cavity and loosened manganese oxide nanosheets, which is different from the above-mentioned architectures.

### 3.3. Electrochemical properties

Research results have found that the specific capacitance of the cathode materials is related to its specific surface area, the electrical conductivity in the solid phase and ionic transport within the pores because the large specific surface area and good ionic transport can lead to a higher current density and facilitate the fast transport of electrolyte with metal ions [48]. Therefore, the manganese oxide based electrode with large specific surface area and suitable pore size shows a promising prospect as supercapacitor electrode

material. Cyclic voltammetry is an important tool to investigate the capacitive behavior of the prepared materials. Because of the low electrical conductivity ( $10^{-5}$ – $10^{-6} \text{ S cm}^{-1}$ ) for bulk manganese oxides, the CV curves generally show quasi-rectangular shape. The cyclic voltammetry curves at a scan rate of  $5 \text{ mV s}^{-1}$  in  $1 \text{ mol L}^{-1} \text{ Na}_2\text{SO}_4$  solution in a voltage of  $-0.2$ – $0.8 \text{ V}$  for three material electrodes are shown in Fig. 7 (above). The shapes of these curves are quasi-rectangular, indicating the ideal electrical double-layer capacitance behavior and fast charging–discharging process characteristic [49]. For manganese oxide hollow star, the value of specific capacitance is  $366 \text{ F g}^{-1}$ , which is obvious larger than those of manganese oxide hollow cube ( $242 \text{ F g}^{-1}$ ) and manganese oxide hollow octahedron ( $257 \text{ F g}^{-1}$ ). The large specific capacitance may be ascribed to the relative large amount of manganese and large specific surface area. Meanwhile, there are no redox peaks in the voltage of  $-0.2$ – $0.8 \text{ V}$ , indicating that three manganese oxide hollow material electrodes prepared by the present method are charged and discharged at a pseudoconstant rate over the complete voltammetric cycle [46]. These results suggest that the specific

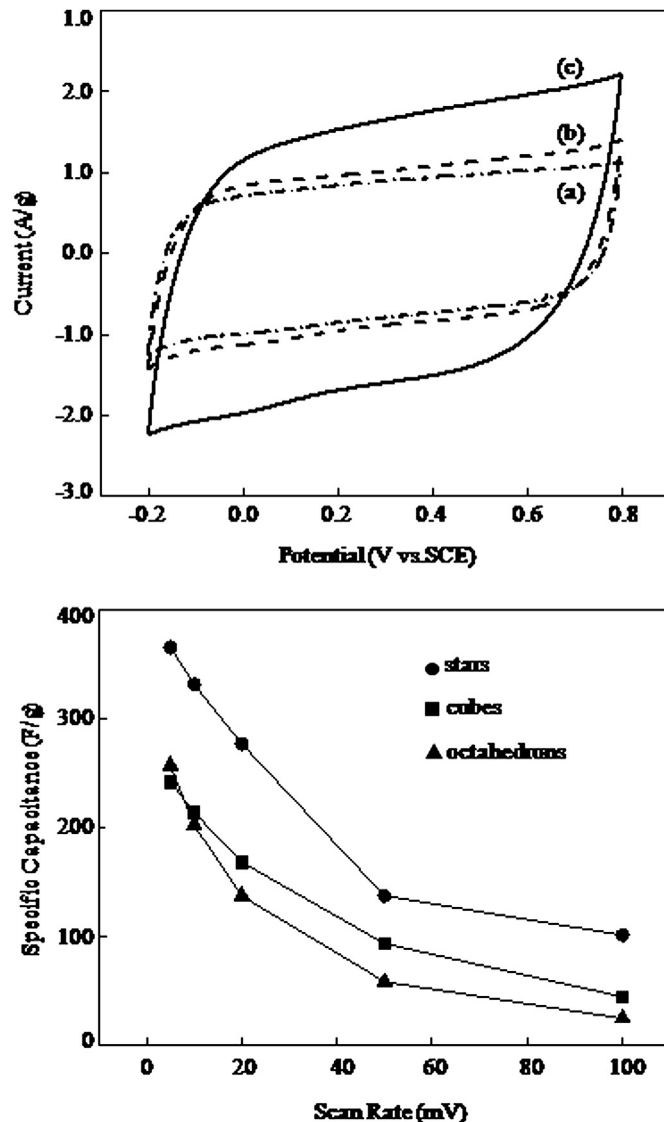


Fig. 7. The CV curves (above) of the manganese oxide hollow structures with different morphologies at a scan rate of  $5 \text{ mV s}^{-1}$  in  $1 \text{ mol L}^{-1} \text{ Na}_2\text{SO}_4$  solution: (a) cubes, (b) octahedrons, and (c) stars, respectively, and the relationship curves between the specific capacitance and the scan rate of CV for the three electrodes (below).

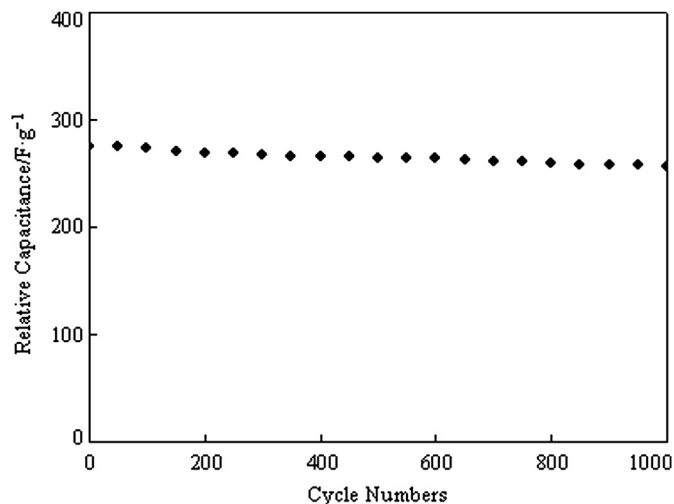


Fig. 8. Variation of the specific capacitance with respect to cycle number. The potential cycling was performed in 1 mol L<sup>-1</sup> Na<sub>2</sub>SO<sub>4</sub> solution within a potential window ranging from -0.2 V to +0.8 V vs Hg/Hg<sub>2</sub>SO<sub>4</sub> at a sweep rate of 20 mV s<sup>-1</sup>.

capacitance of the manganese oxide hollow structures connects with its surface area and the porous structure.

To further evidence the viewpoint that the specific capacitance of manganese oxide hollow structures connects with their surface area and the porous structure, the cyclic voltammetry curves at different scan rates from 5 to 100 mV s<sup>-1</sup> in 1 mol L<sup>-1</sup> Na<sub>2</sub>SO<sub>4</sub> solution in a voltage of -0.2–0.8 V for three electrodes are tested and the relationship between the specific capacitance and the scan rate of CV is shown in Fig. 7 (below). It can be seen that the value of specific capacitance for manganese oxide hollow star is still obvious larger than that of both manganese oxide hollow cube and manganese oxide hollow octahedron at different scan rates, supporting that the specific capacitance of the manganese oxide hollow structures connects with their surface area.

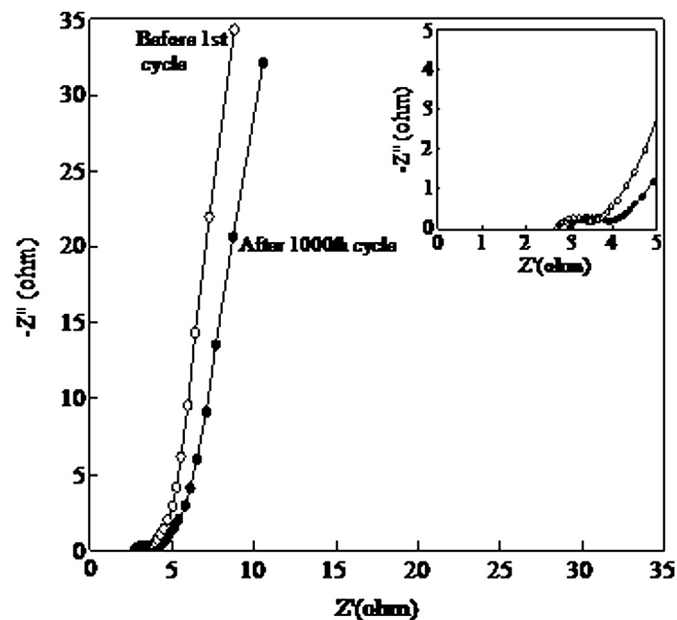


Fig. 9. The electrochemical impedance spectra of the manganese oxide hollow structure electrode with star morphology before 1st and after 1000th cycles in Na<sub>2</sub>SO<sub>4</sub> electrolyte.

Two mechanisms have been proposed for the charge storage for manganese oxide based electrodes. One is intercalation/deintercalation of cations (such as Li<sup>+</sup>, Na<sup>+</sup>, K<sup>+</sup>) or H<sub>3</sub>O<sup>+</sup> into the bulk manganese oxides with concomitant reduction/oxidation of the manganese cations, which is mainly predominant in crystalline manganese oxides. Another is the surface adsorption/desorption of protons or alkali cations from electrolyte and the capacitance depends on the surface area of manganese oxide, which is usually predominant in amorphous manganese oxide [9,41,50]. In the present work, the specific capacitance of the as-prepared amorphous manganese oxide hollow structures connects with their surface areas and the porous structures, thus the redox process is mainly governed by adsorption/desorption of cations in the electrolyte on the amorphous manganese oxides electrode. For manganese oxide hollow star electrode, the large specific capacitance is strongly attributed to the relative large specific surface area and narrow pore size distribution. The large specific surface area provides more possibility of efficient protons/ions diffusion and adsorption/desorption during the redox transitions, which causes the electron transportation between the electrolyte and manganese oxide electrode. Besides, the narrow pore size distribution is also beneficial for the ionic transportation through the electrolyte and enhances the electrochemical performance [51].

The cycling capability or cycling life of the electrode for supercapacitor is another important requirement. The long-term cycle stability of the manganese oxide hollow star electrode is evaluated by repeating the CV test at a relatively high scan rate of 20 mV s<sup>-1</sup> in the potential window ranging from -0.2 to 0.8 V for 1000 cycles. The variation of the specific capacitance as a function of cycle number is presented in Fig. 8. The manganese oxide hollow star electrode can maintain 1000 cycles without significant capacitance loss. The capacitance retention of 93.1% is observed after 1000 cycles, suggesting that the manganese oxide hollow star electrode shows relatively good stability.

The electrochemical impedance spectra of the manganese oxide hollow star electrode before 1st and after 1000th cycles in 1.0 M Na<sub>2</sub>SO<sub>4</sub> electrolyte with a frequent range of 100 kHz–0.01 Hz. are shown in Fig. 9. The two Nyquist plots are similar to each other in shape, consisting of a small semicircle in the high frequency range and an almost ideal straight line in the low frequency range. The semicircle at high frequency range (see the inset in Fig. 9) is corresponds to the charge transfer resistance and can be calculated by extrapolation of the semicircle on the real impedance axis [52], and the intercepts at the real axis is associated with the combination resistance of ionic resistance of electrolyte, intrinsic resistance of active materials, and contact resistance at the active material/current collector interface [53]. It can be seen that the two diameters of the semicircles are less than 1 ohm, suggesting that the manganese oxide hollow star electrode has relatively small charge transfer resistance compared with the other manganese oxides [54,55]. After 1000 cycles, the semicircle diameter and the intercept at the real axis at high frequency range slightly increases while the slope of the diffusion line little decreases, suggesting that the charge transfer resistance, combination resistance and Warburg diffusive resistance of the electrode slightly increases. At lower frequencies, the straight sloping lines along the imaginary axis represent the Warburg diffusive resistance of the electrolyte in the electrode pores and the proton diffusion in the host materials [56]. It can be concluded that the capacitance slightly decreases after 1000 cycles and the manganese oxide hollow star is suitable for supercapacitor electrode.

#### 4. Conclusions

A variety of manganese oxide electrode materials with uniform nonspherical hollow interiors are successfully prepared via



sacrificial template-engaged redox etching of the shape-controlled corresponding Cu<sub>2</sub>O nanocrystals in KMnO<sub>4</sub> solution at room temperature. The as-prepared amorphous manganese oxide hollow star architecture shows not only a large area of 198 m<sup>2</sup> g<sup>-1</sup>, but also an ideal capacitive behavior with a specific capacitance of 366 F g<sup>-1</sup> in a neutral electrolyte system at a scan rate of 5 mV s<sup>-1</sup>. Moreover, this material also exhibits relatively good cycle stability, and the specific capacitance can maintains 93.1% of the initial one after 1000 cycles at a scan rate of 20 mV s<sup>-1</sup>. This bottom-up synthetic approach is highly tailorable and suitable for the preparation of metal oxide hollow structures with different sizes and morphologies.

## Acknowledgment

This work was supported by the National Natural Science Foundation of China (51172137), the Natural Science Key Foundation of Shaanxi Province (2011JZ001), Changjiang Scholars and Innovative Research Team in University (IRT1070) and the Fundamental Research Funds for the Central Universities (GK201101003).

## References

- [1] P. Simon, Y. Gogotsi, *Nat. Mater.* 7 (2008) 845–854.
- [2] S. Sarangapan, B.-V. Tilak, C.-P. Chen, *J. Electrochem. Soc.* 143 (1996) 3791–3799.
- [3] C. Liu, F. Li, L. Ma, H. Cheng, *Adv. Mater.* 22 (2010) E28–E62.
- [4] R. Kötz, M. Carlen, *Electrochim. Acta* 45 (2000) 2483–2498.
- [5] A. Burke, *J. Power Sources* 91 (2000) 37–50.
- [6] D. Wang, F. Li, M. Liu, G. Lu, H. Cheng, *Angew. Chem. Int. Ed.* 47 (2008) 373–376.
- [7] Z. Wu, D. Wang, W. Ren, J. Zhao, G. Zhou, F. Li, H. Cheng, *Adv. Mater.* 20 (2010) 3595–3602.
- [8] S. Hadži-Jordanov, H. Angerstein-Kozłowska, M. Vuković, B.-E. Conway, *J. Electrochem. Soc.* 125 (1978) 1471–1480.
- [9] W. Wei, X. Cui, W. Chen, D.-G. Ivey, *Chem. Soc. Rev.* 40 (2011) 1697–1721.
- [10] L. Athouël, F. Moser, R. Dugas, O. Crosnier, D. Bélanger, T. Brousse, *J. Phys. Chem. C* 112 (2008) 7270–7277.
- [11] R.-N. Reddy, R.-G. Reddy, *J. Power Sources* 132 (2004) 315–320.
- [12] C. Yu, L. Zhang, J. Shi, J. Zhao, J. Gao, D. Yan, *Adv. Funct. Mater.* 18 (2008) 1544–1554.
- [13] C.-C. Hu, T.-W. Tsou, *J. Power Sources* 115 (2003) 179–186.
- [14] S.-E. Chun, S.-I. Pyun, G.-J. Lee, *Electrochim. Acta* 51 (2006) 6479–6486.
- [15] C.-C. Hu, C.-Y. Hung, K.-H. Chang, Y.-L. Yang, *J. Power Sources* 196 (2011) 847–850.
- [16] J.-H. Kim, K.H. Lee, L.J. Overzet, G.S. Lee, *Nano Lett.* 11 (2012) 2611–2617.
- [17] Y.-J. Yang, E.-H. Liu, L.-M. Li, Z.-Z. Huang, H.-J. Shen, X.-X. Xiang, *J. Alloys Compd.* 505 (2010) 555–559.
- [18] X. Dong, W. Shen, J. Gu, L. Xiong, Y. Zhang, H. Li, J. Shi, *J. Phys. Chem. B* 110 (2006) 6015–6019.
- [19] J. Hu, M. Chen, X. Fang, L. Wu, *Chem. Soc. Rev.* 40 (2011) 5472–5491.
- [20] X. Tang, Z.-H. Liu, C. Zhang, Z. Yang, Z. Wang, *J. Power Sources* 193 (2009) 939–943.
- [21] J.-G. Wang, Y. Yang, Z.-H. Huang, *J. Power Sources* 204 (2012) 236–243.
- [22] M. Xu, L. Kong, W. Zhou, H. Li, *J. Phys. Chem. C* 111 (2007) 19141–19147.
- [23] L. Jin, L. Xu, C. Morein, C.-H. Chen, M. Lai, S. Dharmarathna, A. Doble, S.L. Suib, *Adv. Funct. Mater.* 22 (2010) 3373–3382.
- [24] J. Zhao, Z. Tao, J. Liang, J. Chen, *Cryst. Growth Des.* 8 (2008) 2799–2805.
- [25] W. Zhang, C. Zeng, M. Kong, Y. Pan, Z. Yang, *Sens. Actuators B* 162 (2012) 292–299.
- [26] P. Umek, A. Gloter, M. Pregelj, R. Dominko, M. Jagodič, Z. Jagličić, A. Zimina, M. Brzhezinskaya, A. PotočnikChoy, C. Filipič, A. Levstik, D. Arčon, *J. Phys. Chem. C* 113 (2009) 14798–14803.
- [27] K.A.M. Ahmed, K. Huang, *Mater. Chem. Phys.* 133 (2012) 605–610.
- [28] X. He, M. Yang, P. Ni, Y. Li, Z.-H. Liu, *Colloids Surf. A* 363 (2010) 64–70.
- [29] M. Zhou, X. Zhang, J. Wei, S. Zhao, L. Wang, B. Feng, *J. Phys. Chem. C* 115 (2011) 1398–1402.
- [30] N. Chen, K. Wang, X. Zhang, X. Chang, L. Kang, Z.-H. Liu, *Colloids Surf. A* 387 (2011) 10–16.
- [31] L. Wang, Y. Ebina, K. Takada, T. Sasaki, *Chem. Commun.* 40 (2004) 1074–1075.
- [32] K. An, S.G. Kwon, M. Park, H.B. Na, S.I. Baik, J.H. Yu, D. Kim, J.S. Son, Y.W. Kim, I.C. Song, W.K. Moon, H.M. Park, T. Hyeon, *Nano Lett.* 8 (2008) 4252–4258.
- [33] S. Jiao, L. Xu, K. Jiang, D. Xu, *Adv. Mater.* 18 (2008) 1174–1177.
- [34] Z. Wang, D. Luan, F.Y.C. Boey, X.W. Lou, *J. Am. Chem. Soc.* 133 (2011) 4738–4741.
- [35] G. Millazzo, S. Caroli, *Tables of Standard Electrode Potentials*, John Wiley & Sons Inc., New York, 1978.
- [36] D.-Z. Zhang, H. Zhang, L. Guo, K. Zheng, X.-D. Han, Z. Zhang, *J. Mater. Chem.* 19 (2009) 5220–5225.
- [37] D. Wang, M. Mo, D. Yu, L. Xu, F. Li, Y. Qian, *Cryst. Growth Des.* 3 (2003) 717–720.
- [38] J. Yan, T. Wei, W. Qiao, B. Shao, Q. Zhao, L. Zhang, Z. Fan, *Electrochim. Acta* 55 (2010) 6973–6978.
- [39] B. Li, G. Rong, Y. Xie, L. Huang, C. Feng, *Inorg. Chem.* 45 (2006) 6404–6410.
- [40] G.-R. Li, Z.-P. Feng, Y.-N. Qu, D. Wu, R. Fu, Y.-X. Tong, *Langmuir* 26 (2004) 2209–2213.
- [41] M. Toupin, T. Brousse, D. Bélanger, *Chem. Mater.* 16 (2004) 3184–3190.
- [42] M. Chigane, M. Ishikawa, *J. Electrochem. Soc.* 147(6) 2246–2251.
- [43] M. Toupin, T. Brousse, D. Bélanger, *Chem. Mater.* 14 (2002) 3946–3952.
- [44] M.-K. Song, S. Cheng, H. Chen, W. Qin, K.-W. Nam, S. Xu, X.-Q. Yang, A. Bongiorno, J. Bai, T.-A. Tyson, J. Cho, M. Liu, *Nano Lett.* 12 (2012) 3483–3490.
- [45] K.-S.-W. Sing, D.-H. Everett, R.-A.-W. Haul, L. Moscou, R.-A. Pierooti, J. Rouquerol, T. Siemieniewska, *Pure Appl. Chem.* 57 (1985) 603–619.
- [46] H. Chen, J. He, C. Zhang, H. He, *J. Phys. Chem. C* 111 (2007) 18033–18038.
- [47] Y.-F. Lee, K.-H. Chang, C.-C. Hu, Y.-H. Chu, *J. Power Sources* 206 (2012) 469–475.
- [48] L. Shen, X. Zhang, H. Li, C. Yuan, G. Cao, *J. Phys. Chem. Lett.* 2 (2011) 3096–3101.
- [49] Q. Li, Z.-L. Wang, G.-R. Li, R. Guo, L.-X. Ding, Y.-X. Tong, *Nano Lett.* 12 (2012) 3803–3807.
- [50] J.-G. Wang, Y. Yang, Z.-H. Huang, F. Kang, *J. Power Sources* 204 (2012) 236–243.
- [51] J. Ni, W. Lu, L. Zhang, B. Yue, X. Shang, Y. Lv, *J. Phys. Chem. C* 113 (2009) 54–60.
- [52] M. Ghaemi, F. Makhlooghi, H. Adelhkhani, M. Aghazadeh, H.-M. Shiri, *Int. J. Electrochem. Sci.* 5 (2010) 131–146.
- [53] J. Gamby, P. Taberna, P. Simon, J. Fauvarque, M. Chesneau, *J. Power Sources* 101 (2001) 109–116.
- [54] J.-L. Liu, L.-Z. Fan, X. Qu, *Electrochim. Acta* 66 (2012) 302–305.
- [55] Z. Sun, H. Chen, D. Shu, S. Tang, J. Zhang, *J. Power Sources* 203 (2012) 233–242.
- [56] X. Du, P. Guo, H. Song, X. Chen, *Electrochim. Acta* 55 (2010) 4812–4819.